Geophysical Journal International

*Geophys. J. Int.* (2014) **199,** 1910–1918 doi: 10.1093/gji/ggu365
GJI Seismology

# A unified map of Moho depth and $V_p/V_s$ ratio of continental China by receiver function analysis

Rizheng He,[1,2] Xuefeng Shang,[1] Chunquan Yu,[1] Haijiang Zhang[3] and Robert D. Van der Hilst[1]

[1]*Department of Earth, Atmospheric, and Planetary Sciences, Massachusetts Institute of Technology, 77 Massachusetts Avenue, Cambridge, MA 02139, USA*
[2]*Institute of Geology, Chinese Academy of Geological Sciences, 26 Baiwanzhuang Road, Beijing 100037, China*
[3]*Laboratoy of Seismology and Physics of Earth's Interior, School of Earth and Space Sciences, University of Science and Technology of China, 96 Jinzhai Road, Hefei 230026, China. E-mail: zhang11@ustc.edu.cn*

Accepted 2014 September 17. Received 2014 September 14; in original form 2014 June 8

## SUMMARY

Continental China consists of a complex amalgamation of geotectonic units and has experienced strong and widespread tectonic deformation since the Mesozoic. To understand its geological structure better, we conducted a systematic receiver function analysis using a total of 83 509 teleseismic traces in the time period of 2009–2010 recorded by 798 broad-band stations, among which 749 stations are permanent digital seismic stations from China Earthquake Networks Center and 49 stations were temporarily deployed in northern Central Tibet. A standard $H$–$\kappa$ stacking method is employed to determine Moho depth and $V_p/V_s$ ratio underneath each station from teleseismic receiver function analysis. The obtained Moho depth variations are generally consistent with those determined from various deep seismic soundings profiles. We combine our results with those from previous receiver functions studies to produce a high-resolution map of Moho depth and $V_p/V_s$ variation for continental China. Compared to previous studies, the new study concerns many more stations and the resulting Moho depth map has much higher lateral resolution, especially in the eastern China. Overall, the Moho depth variation has a remarkable correlation with major tectonic units in continental China. For example, across the well-known gravity gradient line in east China, there is a clear shift in Moho depths. In general, the map of $V_p/V_s$ ratio shows relatively high anomalies underneath Tibetan Plateau, along the gravity gradient line, and under several volcanoes.

**Key words:** Time-series analysis; Gravity anomalies and Earth structure; Broad-band seismometers; Body waves; Computational seismology; Cratons.



## 1 INTRODUCTION

Continental China has experienced active tectonic activities since the Mesozoic (Ren *et al.* 1997), including deep westward subduction of the Pacific plate (Fukao *et al.* 2001; Huang & Zhao 2006; Li & Van der Hilst 2010), large-scale backarc extension in northeast China, lithosphere removal of the north China craton (NCC; Chen *et al.* 2008), reactivation of the Tan–Lu faults (Yin & Nie 1993), strong Mesozoic magmatism in south China (Li *et al.* 2009) and rapid uplifting of Tibetan plateau (Yin & Harrison 2000). Lateral variations of Moho discontinuity between the crust and upper mantle are considered to document and retain the basic processes in plate tectonic evolution (Meissner 1973; Anderson 2007). Moho depth data thus provide first-order information for the restoration of the complicated geodynamics (Prodehl & Mooney 2012).

There are two main categories of seismic methods to determine Moho depths. One is known as deep seismic sounding (DSS), in which active controlled sources are employed and reflection (or refraction) signals are analysed to infer Moho depth and seismic wave speeds (e.g. Meissner 1973; Prodehl & Mooney 2012). Li *et al.* (2006) compiled a Moho depth map of continental China solely from different DSS profiles. However, due to high cost and complicated logistics of acquisition, most of DSS surveys are along linear profiles and the Moho is not regularly sampled (Li *et al.* 2006; Zhang *et al.* 2011; Prodehl & Mooney 2012). The second category, which includes methods like receiver function (RF) analysis, relies on passive seismic sources, which leads to simpler logistics and is relatively inexpensive. RF analysis has become increasingly popular (Langston 1977; Owens *et al.* 1984; Ammon 1991; Chevrot & Van der Hilst 2000; Zhu & Kanamori 2000) and has been applied, for instance, in northern and northeastern China (Chen *et al.* 2008; Liu & Niu 2011; He *et al.* 2014; Wang *et al.* 2014), eastern Tibet (Xu *et al.* 2007; Zhang *et al.* 2009; Pan & Niu 2011; Sun *et al.* 2012) and southern China (He *et al.* 2013) to map Moho depth variations,

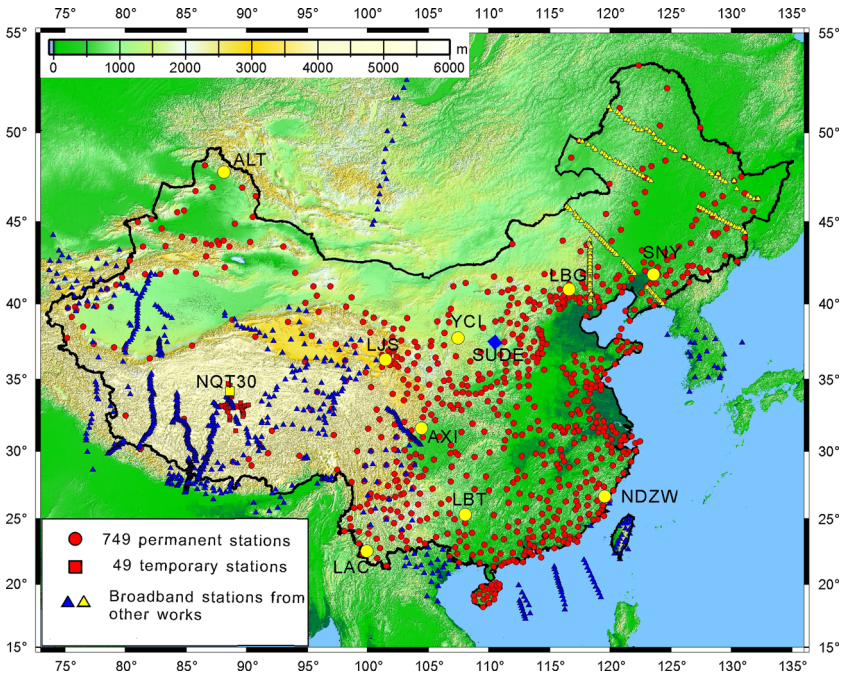


**Figure 1.** Map of station distribution for receiver function studies. The background topography is from GTOPO30 (http://www.webgis.com/terr_world_03.html). Red circles denote 749 permanent stations; red squares are 49 temporal stations; blue triangles depict stations from previous receiver function analysis (see Table S1); yellow triangles depict stations from Li *et al.* (2014). The yellow square indicates a temporary broad-band station in Qiangtang, whose result is shown in Fig. 2. Yellow circles denote nine permanent stations with station name shown in Fig. S1. Blue diamond denotes station SUDE with double interfaces identified in receiver functions.

and, in some cases, Poisson's ratios. Chen *et al.* (2010) endeavoured to map the Moho depth of continental China by RFs, but only 48 permanent stations were used, and because of the limited sampling, only large-scale structures were revealed. Li *et al.* (2014) presented a new crustal thickness map of the continental China by compiling more than 1900 estimates of crustal thickness from previous RF studies. It is noted that RFs are sensitive to velocity contrast across subsurface interfaces. Thus, the Moho from RFs may be different from other techniques, for instance, the virtual DSS method (VDSS, Yu *et al.* 2012), which defines the Moho mainly by absolute velocities, which has advantages when the crustal structure is complicated.

In this paper, we systematically conducted RF analysis for 798 seismographs using teleseismic data recorded in the period of 2009–2010 (Fig. 1). Subjecting data from an unprecedented number of seismic stations to a consistent processing flow and combining our results with those from other RF studies (especially in western China), we are able to yield a unified and detailed map of Moho depth and $V_p/V_s$ ratio of continental China. Compared to previous studies (e.g. Chen *et al.* 2010; Li *et al.* 2014), this is the first time to use a consistent process flow for the RF analysis on a large amount of seismic stations to obtain the Moho depth map of the continental China. The new estimates of Moho depth and $V_p/V_s$ ratio provide important constraints on models of the crust–mantle evolution in continental China (Li *et al.* 2006; Zhang *et al.* 2011).

## 2 DATA AND RF ANALYSIS

RF analysis is routinely applied to teleseismic data to constrain seismic discontinuities in the crust and upper-mantle beneath seismic stations (Langston 1977; Owens *et al.* 1984; Ammon 1991; Chevrot & Van der Hilst 2000; Zhu & Kanamori 2000). The vertical component, considered to contain the source signature, is deconvolved from horizontal components to get RFs. The RFs thus produced emphasize the converted phases (*P*-to-*S* or *S*-to-*P*). In this study, we focus on *P*-wave RFs, consisting of direct *P* wave and its coda. In view of the trade-off between velocity and depth, $H$–$\kappa$ analysis is performed to constrain Moho depth (Zhu & Kanamori 2000).

We collected three-component waveform data from 728 events that occurred in 2009 and 2010 and which were recorded by 879 broad-band permanent stations in China Earthquake Networks Center (CENC, Liu *et al.* 2008) as well as data from 506 events recorded by 53 temporary stations in northern Central Tibet. The epicentral distance varies between 30° and 95°, and the event magnitudes are 5.0 or greater. Niu & Li (2011) noted that many broad-band stations in China had bad orientations and polarities for the period of 2007–2008. These issues were corrected starting from 2009 and thus do not cause troubles in our RF analysis.

Several standard pre-processing steps are applied to get RFs at each station. First, horizontal components are rotated to radial and transverse directions. Only radial components are used in this study. Secondly, noisy and abnormal records including those with likely bad instrument orientations and polarities were removed. About 156 800 traces out of more than 420 000 traces were kept for processing because they had signal-to-noise ratio of 2.0 or higher. Thirdly, the vertical component is deconvolved from the radial component, and a Gaussian filter with a factor of 2.5 (maximum frequency ~1.2 Hz) was applied after deconvolution. Finally, we selected RFs with clear direct *P* and converted phase at Moho (*Ps*), which resulted in a total of 84 800 radial RFs for $H$–$\kappa$ analysis.

The ak135 continental model is used as the reference model for the $H$–$\kappa$ analysis. We choose stacking weights of 0.4, 0.4 and 0.2 for phases *Ps*, *PpPs* and *PpSs+PsPs*, respectively, considering that $H$–$\kappa$ analysis is mainly constrained by the first two. The optimal

crust thickness ($H$) and $V_p/V_s$ ratio ($\kappa$) are determined by searching for the maximum objective function value in the $H$–$\kappa$ domain through a grid search. The range of possible thicknesses ($H$) is from 20 to 80 km and $V_p/V_s$ ratio is allowed to vary between 1.5 and 2.0. Finally, the depth to the Moho is given with respect to the mean sea level.

## 3 RESULTS AND DISCUSSIONS

Fig. 2 shows an example of the RF analysis for a temporary seismic station NQT30 located in Tibetan plateau. The converted *Ps* phase and its crustal reverberation *PpPs* can be identified clearly in the radial RFs (Fig. 2a). The $H$–$\kappa$ analysis gave a 62-km crustal thickness (without station elevation correction) in north Qiangtang (Fig. 1), which is in agreement with the INDEPTH-III DSS profile (Zhao *et al.* 2001). We also illustrate $H$–$\kappa$ analysis results for nine stations (Fig. S1) that are located on the different geological units in continental China shown in Fig. 1. For these nine stations, the Moho depth is well constrained from $H$–$\kappa$ analysis. For details of uncertainty and number of RFs for each station, we refer to Fig. S4.

As shown in Fig. 1, stations are more evenly and densely distributed in the eastern China (east of 95°E). To mitigate poor sampling in western China (west of 95°E), we combine our results (Fig. S2) with previous RFs studies (summarized in Table S1). The Moho depth map of continental China (Fig. 3a) is then obtained by interpolation from Moho depths on individual stations in Table S2, after median averaging (Grochulski *et al.* 1985) and 2-D spherical Green's function spline smoothing (Wessel & Bercovici 1998). For data of Moho depth in continental China with 0.5° grids, we refer to Table S3. We first compare our results with previous DSS studies. Fig. S5 shows to the east of longitude 105°E the differences of Moho

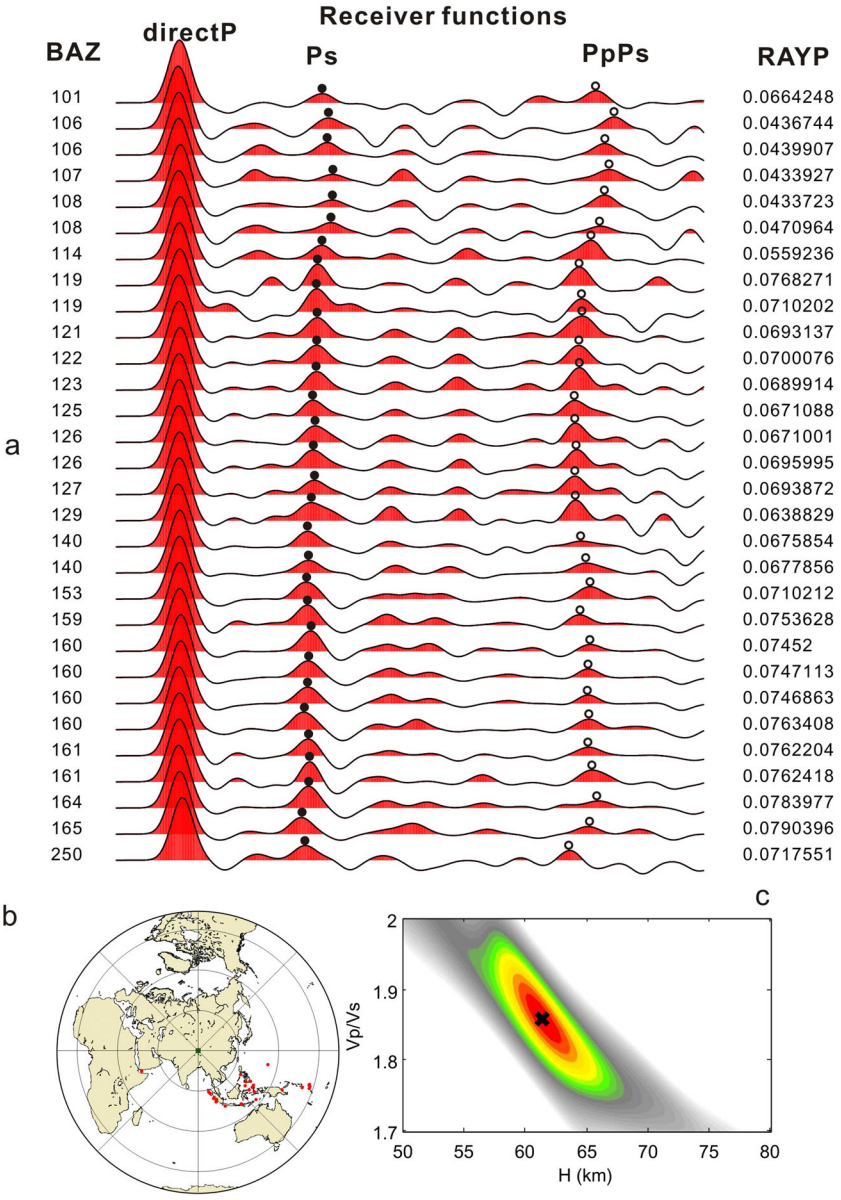


**Figure 2.** An example of receiver function analysis for station NQT30 in northern Tibet. (a) High-quality radial receiver functions. The backazimuths vary from 101° to 250°. Solid circles and open circles mark the arrival times of *Ps* and *PpPs* conversions from the Moho, respectively. RAYP means ray parameter. (b) The distribution of earthquakes (red dots) used in receiver function analysis in (a). (c) $H$–$\kappa$ analysis of station NQT30. The black cross indicates the optimal trade-off point between the crustal thickness and $V_p/V_s$ ratio, which corresponds to the Moho depth of 62 km without elevation correction.

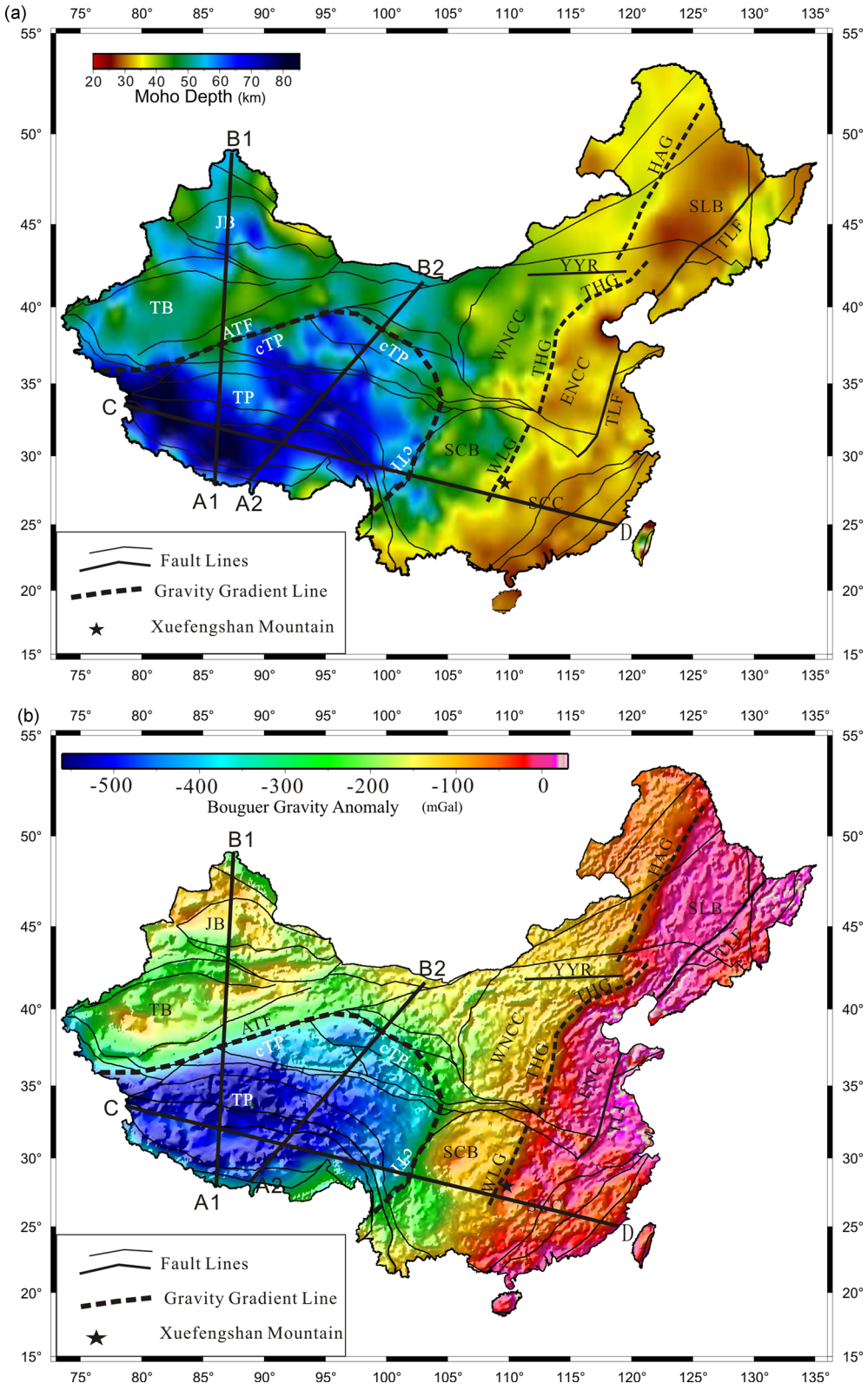


**Figure 3.** Map of (a) Moho depths from this study, (b) Bouguer gravity anomalies (Ma 1989), and (c) $V_p/V_s$ ratios in China. Fault lines are from Gen, S.F., Institute of Geology, Chinese Academy of Geological Sciences (personal communications). HAG, THG and WLG indicate HingAnling, TaiHangshan and WuLingshan gravity gradient belts in east China, respectively. cTP is a circum-Tibetan plateau gravity gradient belt. TLF denotes Tancheng–Lushan strike-slip faults, YYR denotes Yanshan–Yinshan intraplate-orogenic ranges, ATF denotes Altyn Tagh strike-slip faults. SLB—Songliao Basin in Northeastern China, ENCC—Eastern North China Craton, WNCC—Western North China Craton, SCB—Sichuan Basin, SCC—South China Continent, JB—Junggar Basin, TB—Tarim Basin, TP—Tibetan plateau. Cross-sections of A1–B1, A2–B2 and C–D are shown in black lines in (a) and (b).

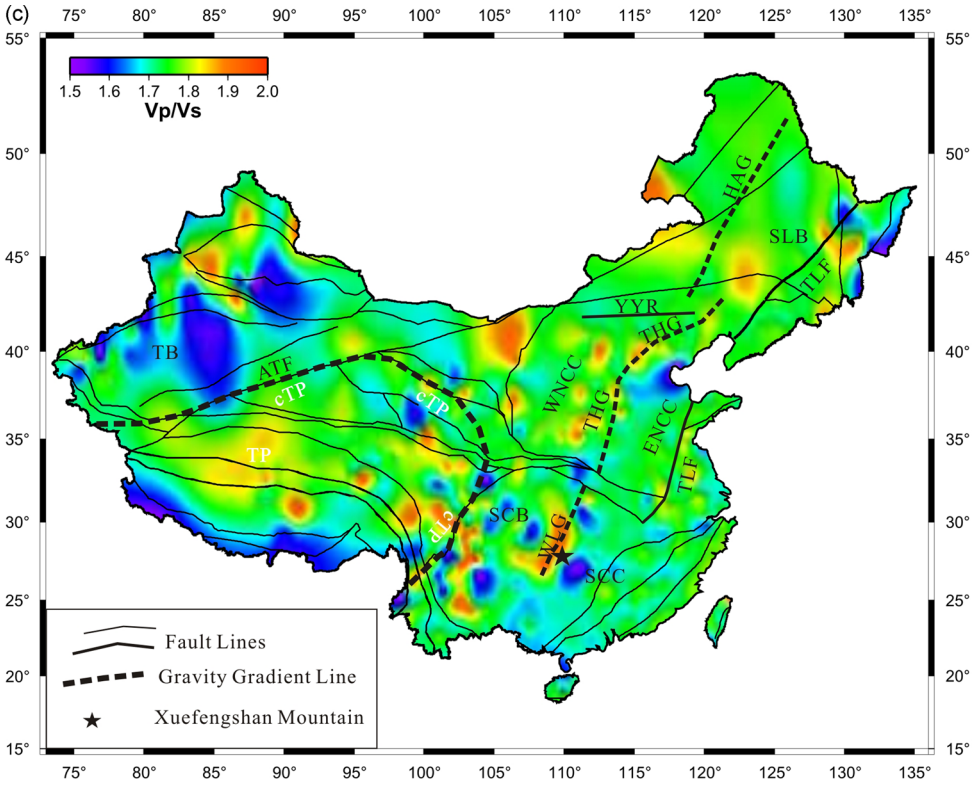


**Figure 3** (*Continued.*)

depth are within 5 km, but to the west of 105°E, the differences are somewhat greater, varying from 5 to 10 km. Differences in Moho depth in excess of 10 km are observed around the boundary of northeastern Tibetan plateau, with steep topography and, possibly, a 15-km vertical offset Moho (Li *et al.* 2006; Zhang *et al.* 2011).

We also compared our Moho depth map with that compiled by Li *et al.* (2014) along the same DSS profiles in northern China (Fig. S6). Note that we also used RF results on temporary broadband stations in northeastern China compiled by Li *et al.* (2014) because of the sparse permanent seismic stations. The standard deviation of the absolute differences between our derived Moho depths and the DSS results in North China is 2.777 km, while it is 3.063 km for the Moho depth in North China by Li *et al.* (2014), indicating overall our Moho depth map is more accurate. This is mainly because we conducted the RF analysis using a consistent process flow. Although Li *et al.* (2014) also adopted certain measures to assess and choose good-quality crustal thickness results from previous studies, there is no guarantee that the RF analysis is conducted in the same manner for different studies.

A remarkable variation of Moho depth (from 30 km to 80 km) is observed across continental China (Fig. 3a). In general, variations in Moho depth are negatively correlated with surface topography (Fig. 1) and positively with Bouguer gravity anomalies (Fig. 3b). Two gravity gradient lines with −100 mGal offset are marked as HingAnling–TaiHangshan–WuLingshan gravity gradient line (HAG-THG-WLG) in east China and a circum-Tibetan plateau (cTP) gravity gradient belt (Fig. 3). The two belts generally divide Moho topography into three steps of terrace. Across the HAG-THG-WLG, from east to west, the Moho depth varies sharply from ∼30 to ∼40 km. Inside the Tibetan plateau, the average Moho depth is about 60 km. Moho topography clearly delineates the boundaries of large-scale basins in China, such as Songliao basin (SLB), Tarim basin (TB) and Sichuan basin (SCB).

In northern China, Bouguer gravity anomalies reveal that the northeastern-striking HAG and THG are separated by the east–west trending Yinshan–Yanshan Ranges (YYR; Fig. 3b), which are considered as a Mesozoic intraplate orogeny (Wang *et al.* 2011). However, the Moho depth map suggests that HAG links to THG as the coherent Moho slope (Fig. 3a). In NCC, the Moho becomes shallower from ∼45 km in western NCC to ∼30 km in eastern NCC, separated by THG. Yu *et al.* (2012) found two interfaces near the eastern margin of the western NCC using a denser seismic array, one at ∼45-km depth and the other at ∼60-km depth. They interpreted the deeper one as the Moho and the shallower one as the Conrad discontinuity based on absolute velocities. DSS result around here (Teng *et al.* 2010) also reported two interfaces at roughly same depths as Yu *et al.* (2012); however, Teng *et al.* (2010) interpreted the shallower one as the Moho. In the same study region as Yu *et al.* (2012), we also found double interfaces in RFs from teleseismic events at different azimuths (Fig. S1b). We pick the shallower one as the Moho to be consistent with interpretations elsewhere, but the difference does indicate the possibility that interpretations can be ambiguous. Moreover, continuing Mesozoic and Cenozoic activity on the Tan–Lu fault caused Moho depth changes, which is well consistent with observations along a temporary seismic array (Chen *et al.* 2008).

South of NCC, the Moho depth map shows that the Moho has an evident offset of ∼6 km from THG to WLG. The offset is associated with the east Qinling–Dabieshan ultra-high pressure metamorphic zone observed on the surface (Bader *et al.* 2013), which was caused by northward subduction of the South China block beneath the NCC in Triassic times (Dong *et al.* 2008). Beneath the WLG segment of the South China block, the Moho depth varies at 5–10 km, and on the surface, this segment correlates with the Xuefengshan uplifting tectonic zone (Zhang *et al.* 2013). The consistency of our Moho depth variations with major tectonic units is further illustrated in

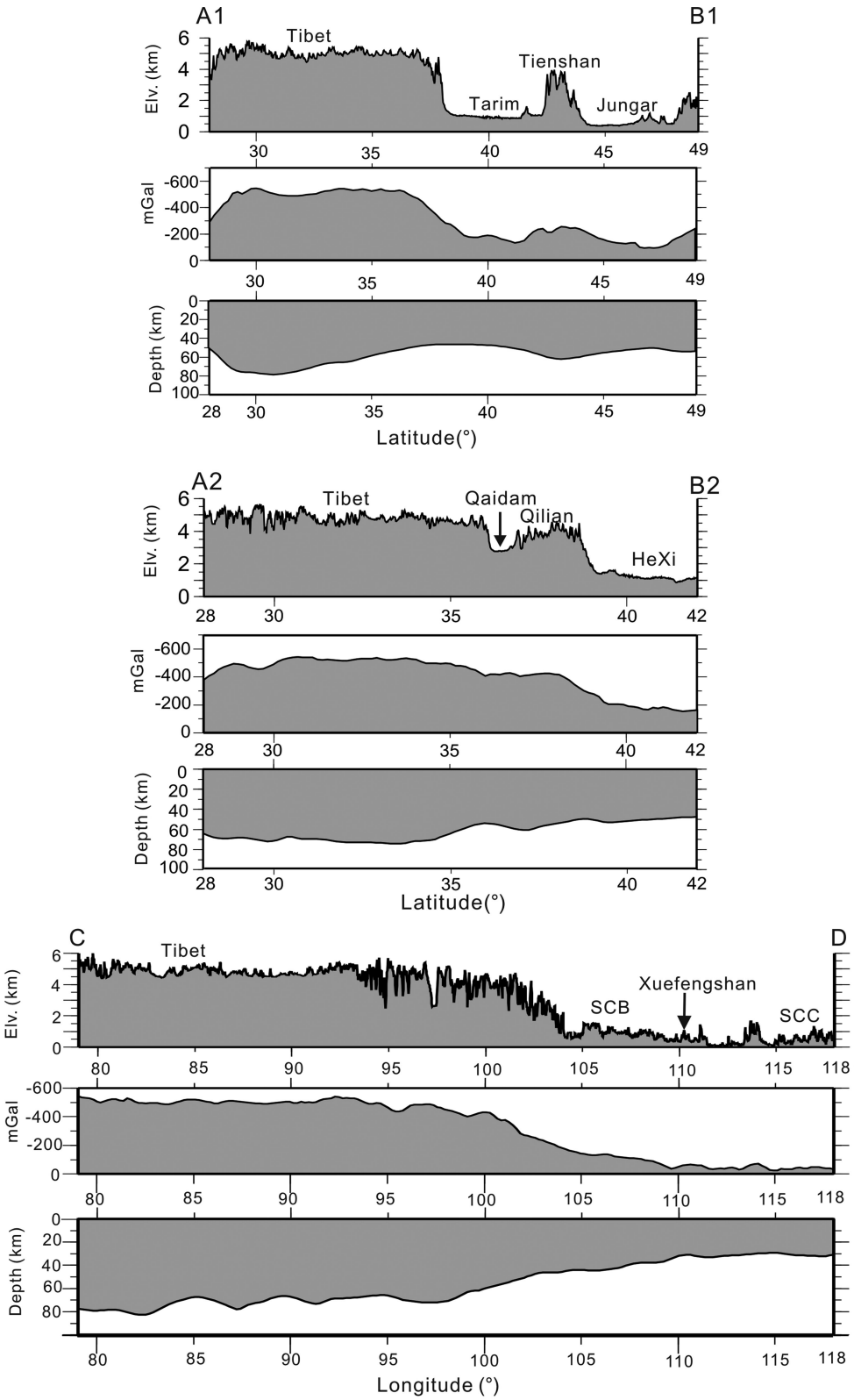


**Figure 4.** Cross-sections of topography, Bouguer gravity anomaly and Moho depth (shown at top, middle and bottom in each subplot, respectively) along A1–B1, A2–B2 and C–D lines shown in Fig. 3(a).

three cross-sections (Fig. 4). In the cross-section through western Tibetan Plateau, TB and Junggar Basin, Moho depth gradually decreases from ∼80 to ∼50 km around the boundary between Tibetan Plateau and TB, stays nearly the same beneath TB and then becomes deeper beneath Tienshan Mountain (Fig. 4a). For the cross-section A2–B2, it shows that the Moho depth becomes shallower beneath Qaidam Basin after passing central Tibetan Plateau, and then is deeper again beneath Qilian Mountain (Fig. 4b). For the northwest–

southeast cross-section C–D passing through Tibetan Plateau, SCB, WLG and south China craton, the Moho depth generally correlates with the topography (Fig. 4c). These three cross-sections also clearly demonstrate that Moho depth variations generally correlate with Bouguer gravity anomalies in that the greater gravity anomalies are the deeper Moho (Fig. 4). The remarkable coincidence between the surface structure and the sharp change of the Moho depth indicates that the Moho of a continent with a stable lithosphere, indeed, could record and preserve tectonic evolution information (Meissner 1973). However, Moho with an average of 30 km in southeast China suffered from intrusion of wide-spread magmatism since Mesozoic times (Li *et al.* 2009), which may affect the current Moho topography.

In this study, the $V_p/V_s$ ratios are determined through the $H$–$\kappa$ analysis of RFs by assuming a constant crustal $V_p$ model of 6.3 km s$^{-1}$. Therefore, the map of $V_p/V_s$ ratio (Fig. 3c) only represents the average value beneath each station. Nonetheless, $V_p/V_s$ variations still correlate with some major tectonic features in continental China. For example, some volcanoes such as Wudalianchi volcano, Changbaishan volcano and Tengchong volcano are associated with high $V_p/V_s$ anomalies. Tomographic studies have shown that beneath these volcanoes, there exist low velocity anomalies, likely caused by partial melting (Lei *et al.* 2013), which would correspond to high $V_p/V_s$ anomalies as found in this study. Overall, the Tibetan Plateau is associated with high $V_p/V_s$ anomalies, consistent with the likely existence of thermal flow zone within the crust from seismic anisotropy (Shapiro *et al.* 2004), and low $V_s$ anomalies identified in ambient noise tomographic results (Yang *et al.* 2010; Yao *et al.* 2010). In East China, high $V_p/V_s$ anomalies could be resulted from magmatism (Zhao *et al.* 2011), such as volcano eruption and granite intrusion. It is also noted that the gravity gradient line HAG-THG-WLG is associated with high $V_p/V_s$ anomalies.

## 4 CONCLUSIONS

By combining a systematic RF analysis for 798 stations with previously reported measurements, we obtained an unprecedented high-resolution crustal thickness map of continental China. The Moho depth map from our study is generally consistent with local DSS results but has a better spatial coverage. Overall, the Moho topography in continental China correlates positively with the Bouguer gravity anomaly map and negatively with surface topography. The two areas associated with sharp changes in Moho depth correspond well with the gravity gradient belts, delineating three steps of terrace in Moho topography from ~30 to ~40 km to 50–60 km in depth. In addition, the map of average crustal $V_p/V_s$ variation obtained from RF analysis also correlates well with some tectonic features. Overall, the map of Moho depth and $V_p/V_s$ variation obtained in this study is useful for better understanding the crust–mantle evolution in continental China.

## ACKNOWLEDGEMENTS

Waveform data used in this study were provided by CENC and Project TITAN, which are greatly appreciated. All the figures in the paper are made by using the GMT software package distributed by Wessel & Smith (1995). This work was supported partly by grants from Experiment and Integration of Deep Probe Techniques in China (SinoProbe-02, 201011044), the Natural Science Foundation of China (40774051, 40974060, and 41274095), the Basic outlay of scientific research work from the Ministry of Science and Technology, China (J1216) and also by DE-NA0001523 from the U.S. Department of Energy (RvdH).

## REFERENCES

Anderson, D.L., 2007. *New Theory of the Earth,* Cambridge Univ. Press, 384 pp.

Ammon, C.J., 1991. The isolation of receiver effects from teleseismic P waveforms, *Bull. seism. Soc. Am.,* **81,** 2504–2510.

Bader, T., Ratschbacher, L., Franz, L., Yang, Z., Hofmann, M., Linnemann, U. & Yuan, H., 2013. The heart of China revisited, I. Proterozoic tectonics of the Qin moutains in the core of supercontinent Rodinia, *Tectonics,* **32,** 661–687.

Chang, S.-J. & Baag, C.-E., 2007. Moho depth and crustal $V_p/V_s$ variation in Southern Korea from teleseismic receiver functions: implication for tectonic affinity between the Korean Peninsula and China, *Bull. seismic. Soc. Am.,* **97,** 1621–1631.

Chen, L., Wang, T., Zhao, L. & Zheng, T., 2008. Distinct lateral variation of lithosphere thickness in the northeastern north China craton, *Earth planet. Sci. Lett.,* **267,** 56–68.

Chen, Y., Niu, F., Liu, R., Huang, Z., Tkalčić, H., Sun, L. & Chan, W., 2010. Crustal structure beneath China from receiver function analysis, *J. geophys. Res.,* **115**(B3), B03307, doi:10.1029/2009JB006386.

Chevrot, S. & Van der Hilst, R.D., 2000. The Poisson's ratio of the Australian crust: geological and geophysical implications, *Earth planet. Sci. Lett.,* **183,** 121–132.

Dong, S.W., Li, Q.S., Gao, R., Liu, F.T., Xu, P.F., Liu, X.C. & Guan, Y., 2008. Moho-mapping in the Dabie ultrahigh-pressure collisional orogen, central China, *Am. J. Sci.,* **308**(4), 517–528.

Fukao, Y., Widiyantoro, S. & Obayashi, M., 2001. Stagnant slabs in the upper and lower mantle transition region, *Rev. Geophys.,* **39,** 291–323.

Grochulski, W., Mitraszewski, P. & Penczek, P., 1985. Application of combined median-averaging filters to scintigraphic image processing, *Nuklearmedizin,* **24**(4), 164–168.

He, C.S., Donga, S.W., Santosh, M. & Chen, X.H., 2013. Seismic evidence for a geosuture between the Yangtze and Cathaysia Blocks, South China, *Sci. Rep.,* **3,** 2200, doi:10.1038/srep02200.

He, C.S., Dong, S.W., Chen, X.H., Santosh, M. & Li, Q.S., 2014. Crustal structure and continental dynamics of Central China: a receiver function study and implications for ultrahigh-pressure metamorphism, *Tectonophysics,* **610,** 172–181.

Huang, J. & Zhao, D., 2006. High-resolution mantle tomography of China and surrounding regions, *J. geophys. Res.,* **111,** B09305, doi:10.1029/2005JB004066.

Langston, C.A., 1977. The effect of planar dipping structure on source and receiver responses for constant ray parameter, *Bull. seism. Soc. Am.,* **67,** 1029–1050.

Lei, J., Xie, F., Fan, Q. & Santosh, M., 2013. Seismic imaging of the deep structure under the Chinese volcanoes: an overview, *Phys. Earth planet. Inter.,* **224,** 104–123.

Li, C. & Van der Hilst, R.D., 2010. Structure of the upper mantle and transition zone beneath Southeast Asia from traveltime tomography, *J. geophys. Res.,* **115,** B07308, doi:10.1029/2009JB006882.

Li, S.L., Mooney, W.D. & Fan, J., 2006. Crustal structures of mainland China from deep seismic sounding data, *Tectonophysics,* **420,** 239–252.

Li, X.H., Li, W.X., Li, Z.X., Lo, C.H., Wang, J., Ye, M.F. & Yang, Y.H., 2009. Amalgamation between the Yangtze and Cathaysia Blocks in South China: constraints from SHRIMP U-Pb zircon ages, geochemistry and Nd-Hf isotopes of the Shuangxiwu volcanic rocks, *Precambrian Res.,* **174,** 117–128.

Li, Y.H., Gao, M. & Wu, Q., 2014. Crustal thickness map of the Chinese mainland from teleseismic receiver functions, *Tectonophysics,* **610,** 51–60.

Liu, H. & Niu, F., 2011. Receiver function study of the crustal structure of Northeast China: seismic evidence for a mantle upwelling beneath the

eastern flank of the Songliao Basin and the Changbaishan region, *Earthq. Sci.,* **24**(1), 27–33.
Liu, R.F., Gao, J.C., Chen, Y.T., Wu, Z.L., Huang, Z.B., Xu, Z.G. & Sun, L., 2008. Construction of China digital seismic network and development, *Acta seism. Sinica,* **5,** 533–539 (in Chinese with English abstract).
Ma, X.Y., Editorial Board for Lithospheric Dynamics Atlas of China State Seismological Bureau, 1989. *Lithospheric Dynamics Atlas of China,* China Cartographic Publishing House, pp. 8–9 (in Chinese with English abstract).
Meissner, R., 1973. The 'MOHO' as a transition zone, *Geol. Surveys,* **1,** 195–216.
Nguyen, V.-D., Huang, B.-S., Le, T.-S., Dinh, V.-T., Zhu, L. & Wen, K.-L., 2013. Constraints on the crustal structure of northern Vietnam based on analysis of teleseismic converted waves, *Tectonophysics* **601,** 87–97.
Niu, F. & Li, J., 2011. Component azimuth of the CEArray stations estimated from P-wave particle motion, *Earthq. Sci.,* **24**(1), 3–13.
Owens, T.J., Zandt, G. & Taylor, S.R., 1984. Seismic evidence for an ancient rift beneath the Cumberland plateau, Tennessee: a detailed analysis of broadband teleseismic p waveforms, *J. geophys. Res.,* **89,** 7783–7795.
Pan, S. & Niu, F., 2011. Large contrasts in crustal structure and composition between the Ordos plateau and the NE Tibetan plateau from receiver function analysis, *Earth planet. Sci. Lett.,* **303**(3), 291–298.
Prodehl, C. & Mooney, W., 2012. Exploring the Earth's crust-history and results of controlled-source seismology, *Geol. Soc. Am. Memoirs,* **208,** 7–46.
Ren, J., Wang, Z., Chen, B., Jiang, C., Niu, B., Li, J., Xie, G., He, Z. & Liu, Z., 1997. A new generation tectonic map of China, *Regional Geol. China,* **16,** 225–230 (in Chinese with English abstract).
Shapiro, N.M., Ritzwoller, M.H., Molnar, P. & Levin, V., 2004. Thinning and flow of Tibetan crust constrained by seismic anisotropy, *Science,* **305**(5681), 233–236.
Sun, Y., Niu, F., Chen, Y. & Liu, J., 2012. Crustal structure and deformation of the SE Tibetan plateau revealed by receiver function data, *Earth planet. Sci. Lett.,* **349,** 186–197.
Teng, J.W. *et al.*, 2010. Velocity structure of layered block and deep dynamic process in the lithosphere beneath the Yinshan orogenic belt and Ordos Basin, *Chinese J. Geophys.,* **53,** 67–85 (in Chinese with English abstract).
Wang, H.-L., Chen, H.-W. & Zhu, L., 2010. Constraints on average Taiwan reference Moho discontinuity Model-receiver function analysis using BATS data, *Geophys. J. Int.,* **183,** 1–19.
Wang, C., Sandvol, E., Zhu, L., Lou, H., Yao, Z. & Luo, X., 2014. Lateral variation of crustal structure in the ordos block and surrounding regions, North China, and its tectonic implications, *Earth planet. Sci. Lett.,* **387,** 198–211.
Wang, T., Zheng, Y., Zhang, J., Zeng, L., Donskaya, T., Guo, L. & Li, J., 2011. Pattern and kinematic polarity of late Mesozoic extension in continental NE Asia: perspectives from metamorphic core complexes, *Tectonics,* **30,** TC6007, doi:10.1029/2011TC002896.
Wessel, P. & Bercovici, D., 1998. Interpolation with splines in tension: a Green's function approach, *Math. Geol.,* **30**(1), 77–93.
Wessel, P. & Smith, W., 1995. New version of the Generic Mapping Tools (GMT) version 3.0 released, *EOS, Trans. Am. geophys. Un.,* **76,** 329.
Xu, L., Rondenay, S. & Van der Hilst, R.D., 2007. Structure of the crust beneath the southeastern Tibetan Plateau from teleseismic receiver functions, *Phys. Earth planet. Inter.,* **165,** 176–193.
Xu, Q., Zhao, J., Pei, S. & Liu, H., 2013. Distinct lateral contrast of the crustal and upper mantle structure beneath northeast Tibetan plateau from receiver function analysis, *Phys. Earth planet. Inter.,* **217,** 1–9.
Yang, Y. *et al.*, 2010. Rayleigh wave phase velocity maps of Tibet and the surrounding regions from ambient seismic noise tomography, *Geochem. Geophys. Geosyst.,* **11,** Q08010, doi:10.1029/2010GC003119.
Yao, H., van der Hilst, R.D. & Montagner, J.P., 2010. Heterogeneity and anisotropy of the lithosphere of SE Tibet from surface wave array tomography, *J. geophys. Res., Solid Earth* (1978–2012), **115**(B12), doi:10.1029/2009JB007142.
Yin, A. & Nie, S., 1993. An indentation model for the North and South China collision and the development of the Tan-Lu and Honam fault systems, East Asia, *Tectonics,* **12,** 801–813.
Yin, A. & Harrison, T.M., 2000. Geologic evolution of the Himalayan–Tibetan orogeny, *Annu. Rev. Earth planet. Sci.,* **28,** 211–280.
Yu, C.-Q., Chen, W.-P., Ning, J.-Y., Tao, K., Tseng, T.-L., Fang, X.D., Chen, Y.J. & Van der Hilst, R.D., 2012. Thick crust beneath the Ordos Plateau: implications for instability of the north China craton, *Earth planet. Sci. Lett.,* **357–358,** 366–375.
Zhang, Z., Wang, Y., Chen, Y., Houseman, G.A., Tian, X., Wang, E. & Teng, J., 2009. Crustal structure across Longmenshan fault belt from passive source seismic profiling, *Geophys. Res. Lett.,* **36,** L17310, doi:10.1029/2009GL039580.
Zhang, Z., Yang, L., Teng, J. & Badal, J., 2011. An overview of the earth crust under China, *Earth Sci. Rev.,* **104,** 143–166.
Zhang, G. *et al.*, 2013. Tectonics of South China continent and its implications, *Sci. China: Earth Sci.,* **56,** doi:10.1007/s11430-013-4679-1.
Zhao, D., Yu, S. & Ohtani, E., 2011. East Asia: seismotectonics, magmatism and mantle dynamics, *J. Asian Earth Sci.,* **40**(3), 689–709.
Zhao, W. *et al.*, 2001. Crustal structure of the central Tibet as derived from project INDEPTH wide-angle seismic data, *Geophys. J. Int.,* **145,** 486–498.
Zhu, L. & Kanamori, H., 2000. Moho depth variation in southern California from teleseismic receiver functions, *J. geophys. Res.,* **105,** 2969–2980.

## SUPPORTING INFORMATION

Additional Supporting Information may be found in the online version of this article:

**Figure S1.** *H–κ* stacking results for nine permanent stations (a) and receiver functions at station SUDE from teleseismic events at different azimuths (b). Station locations are shown as yellow circles in Fig. 1. The optimal solution for the grid search is indicated by a black circle. The top three stations of SNY, LBG and NDZW are located in East China. The middle three stations of ALT, YCI and LBT are located in Northwestern and Middle China, which clearly show the Moho depth change from 50 to 35 km. The bottom three stations of LJS, AXI and LAC are located in eastern margin of the circum-Tibetan gravity gradient line.
**Figure S2.** Map of Moho depth obtained from 749 permanent stations and 49 temporary stations from this study. Crosses mark the locations of 798 stations as controlled points for interpolation. Major tectonic lines are shown in white.
**Figure S3.** Map of 960 $V_p/V_s$ control points for interpolation from this study and other studies. Crosses mark the locations of 798 stations from this study and circles denote 162 $V_p/V_s$ values from other studies (Chang & Baag 2007; Xu *et al.* 2007, 2013; Zhang *et al.* 2009; Wang *et al.* 2010; Lei *et al.* 2013; Nguyen *et al.* 2013). Major tectonic lines are shown in grey.
**Figure S4.** Distribution of standard deviation of Moho depth and the number of receiver functions for stations used in this study. Circle colour denotes standard deviation of Moho depth from *H–κ* stacking. Green, yellow and red denote the standard deviations less than 1.2 km, between 1.2 and 2.0 km and over 2.0 km, respectively. Circle size denotes the number of receiver functions selected for analysis on each station. There are 190 stations with fewer than 50 receiver functions analysed, 227 stations with 50–110 receiver functions analysed and 381 stations with over 110 receiver functions analysed, respectively.
**Figure S5.** Comparison of Moho depths along the DSS profiles with our receiver function analysis results. Green, yellow, red and black indicate the Moho depth differences less than 3 km, between 3 and 5 km, between 5 and 10 km and over 10 km, respectively.
**Figure S6.** Comparison of Moho depths along the DSS profiles in northern China for (a) our receiver function analysis results and

(b) those of Li *et al.* (2014). Blue squares indicate broad-band seismic stations with Moho depths available. Green, yellow, red and black indicate the Moho depth differences less than 3 km, between 3 and 5 km, between 5 and 10 km and over 10 km, respectively.

**Table S1.** Data sources for Moho depths used for interpolation.

**Table S2.** Data set of Moho depth and $V_p/V_s$ ratio of each station in continental China obtained from this study. The first column is latitude, the second is longitude, the third is Moho depth (km) and the last is $V_p/V_s$ ratio.

**Table S3.** Data set of Moho depth with $0.5^\circ \times 0.5^\circ$ grids of continental China obtained from this study. The first column is longitude, the second is latitude and the last is Moho depth (km) with respect to the sea level. NaN means null value for Moho depth (http://gji.oxfordjournals.org/lookup/suppl/doi:10.1093/gji/ggu365/-/DC1).

Please note: Oxford University Press is not responsible for the content or functionality of any supporting materials supplied by the authors. Any queries (other than missing material) should be directed to the corresponding author for the article.